



Full Length Article

Efficient synthesis of monolayer carbon nitride 2D nanosheet with tunable concentration and enhanced visible-light photocatalytic activities



Qiuyan Lin^a, Li Li^a, Shijing Liang^{a,b,*}, Minghua Liu^a, Jinhong Bi^{a,b}, Ling Wu^b

^a Department of Environmental Science and Engineering, Fuzhou University, Minhou, Fujian, 350108, PR China

^b State Key Laboratory of Photocatalysis on Energy and Environment, Fuzhou University, Fuzhou 350002, PR China

ARTICLE INFO

Article history:

Received 19 May 2014

Received in revised form 21 July 2014

Accepted 25 July 2014

Available online 4 August 2014

Keywords:

C₃N₄ nanosheet

Monolayer

Mixed solvents

Tunable concentration

Photocatalytic activity

ABSTRACT

A versatile and scalable mixed solvent strategy was developed to prepare monolayer C₃N₄ nanosheets with tunable concentration for the first time. This approach could also be used to prepare other 2D nanosheets from their layered materials (such as MoS₂, BN, WS₂ etc.). The structural features and intrinsic semiconductor properties of the as-prepared C₃N₄ nanosheets have been investigated in detailed. The photocatalytic activities were evaluated by photocatalytic oxidation of both benzyl alcohol and rhodamine B (RhB) under visible light irradiation. Results showed that the as-prepared monolayer C₃N₄ nanosheets with thickness of 0.4 nm still retained the structural features of g-C₃N₄ layer. The functionalities of C₃N₄ nanosheets well inherited from the layered parent counterpart. Furthermore, due to the exceptionally high 2D anisotropy, C₃N₄ nanosheets showed the distinctive physicochemical properties and unique electronic structures, such as high surface area, lower surface defects, stronger reduction ability of the photogenerated electrons, increased photoelectric response, and promoted the charge-carrier migration and separation. All of these favorable factors co-contributed to the greatly improved photocatalytic activities over C₃N₄ nanosheets compared with those of its bulk counterpart.

© 2014 Elsevier B.V. All rights reserved.

1. Introduction

Two-dimensional (2D) nanosheets with molecular thickness have attracted tremendous attention in heterogeneous catalysis [1–3], electronics [4–6], sensors [7], and energy storage [8,9]. Generally, they are prepared by the exfoliation of layered materials [10–12], resulting in that their functionalities could inherit from the layered parent compounds. Furthermore, these 2D nanosheets also exhibit novel electronic structures and distinctive physicochemical properties owing to the exceptionally high 2D anisotropy [13,14]. For example, very recently, we have designed a coupled HNb₃O₈ 2D nanosheet and benzylic alcohols system for visible-light-induced aerobic oxidation of alcohols to corresponding aldehydes with high selectivity [3]. Due to the molecular thickness, large surface area, low surface defects, high photoexcited charge carriers separation rate, abundant Lewis acid sites, strong Brønsted acidity, and a high concentration of surface complexes, the monolayer nanosheet exhibited an amazingly improved photocatalytic activity versus its

layered parent HNb₃O₈. However, our knowledge regarding on how to efficiently synthesize the 2D nanosheets and how to adequately harness the unique performances of the 2D nanosheets is far from satisfactory.

Graphitic carbon nitride (g-C₃N₄), a typical graphite-like layered material, is regarded as a kind of promising photocatalyst for the water splitting and degradation of organic pollutants under sunlight irradiation [15–17]. However, it is worth noting that bulk g-C₃N₄ photocatalyst shows a low photocatalytic activity by far. This may be ascribed to the fact that bulk g-C₃N₄ was typically synthesized by high-temperature and high-pressure routes using melamine and cyanamide as precursor [18,19]. As a result, a vast grain boundary defects would be formed and subsequently the photoexcited charge carriers would recombine at a relatively high rate. Although many strategies have been used to improve the photoactivity [20–25], it is to be said that at present the quantum efficiency is still rather low.

Encouraged by the reported 2D nanosheet photocatalysts, if layered g-C₃N₄ was prepared into the mono- or few-layer C₃N₄ sheets, it could be expected that the photocatalytic activity of carbon nitride would be greatly improved. For example, Liu and co-workers have developed a post-thermal treatment method to

* Corresponding author. Tel./fax: +86 591 22866070.

E-mail address: sjliang2011@gmail.com (S. Liang).



Fig. 1. Schematic illustration of mixed solvent exfoliation process from layered g-C₃N₄ powders to C₃N₄ nanosheets with molecular thickness.

reduce the dimension of g-C₃N₄ [26]. As a result, the as-prepared C₃N₄ showed much superior photocatalytic activities than the bulk parent g-C₃N₄ under visible light irradiation. Notably, this method still has some disadvantages, such as the formation of the interface defects during the calcination process, the reduction of the photoabsorption ability, the relatively thick nanosheet, and the poor yield (< 6%). These are not conducive to the photocatalytic reactions. Although the exfoliation of high quality C₃N₄ 2D nanosheet with low defects could also be achieved mechanically on a small scale, a simple liquid exfoliation method would allow the formation of 2D nanosheets in large quantities. Some researchers have developed some liquid exfoliation methods inspired by the preparation of graphene to fabricate few-layered C₃N₄ nanosheets [27–33]. Unfortunately, the concentration of the as-prepared C₃N₄ nanosheets suspension is very low (below 0.3 mg/mL) [27] and the monolayered C₃N₄ nanosheet is limited [32]. What is worse, the planar atomic structure may also be seriously destroyed in the exfoliation process [26]. These may be caused by the fact that the C₃N₄ nanosheet layer was cohered by covalent bonding and hydrogen bonding [34], which is definitely different from the planar pure covalent bonding cohesion of the graphene. Therefore, it is necessary to develop a novel, facile, and rapid route to fabricate the C₃N₄ nanosheets with molecular thickness in a high concentration because a number of applications exist where nanosheets will be required in large quantities.

Herein, we have developed a versatile and scalable mixed solvent strategy for liquid exfoliation of bulk g-C₃N₄ to produce monolayered C₃N₄ nanosheets for the first time (as shown in Fig. 1). By simply changing the volume ratio of solvents, the concentration of the C₃N₄ nanosheets would be tunable (0.1–3 mg/mL). More importantly, the exfoliated nanosheets could be stabilized against reaggregation for more than half year. The physicochemical properties of the products were characterized in detail. The photocatalytic activities of the as-prepared C₃N₄ nanosheet were evaluated by the selective oxidation of benzyl alcohol and the degradation of RhB under visible light irradiation compared with the layered counterpart. The origin of the improved photocatalytic activity of C₃N₄ nanosheet was also discussed.

2. Experimental

2.1. Synthesis of photocatalysts

All chemical reagents were of analytical grade agents and purchased from Sinopharm Chemical Reagent Co. Ltd. without further purification. Bulk g-C₃N₄ powder was synthesized following the previous paper [16]. In a typical procedure, 10 g melamine was heated at 550 °C for 4 h in static air with a heating rate of 2.3 °C/min. After cooling naturally, the resultant yellow agglomerates were milled into powder in an agate mortar for further use.

The graphene-like C₃N₄ 2D nanosheets were prepared by a mixed-solvent exfoliation method. In detail, 500 mg of bulk g-C₃N₄ powders were added into 150 mL solvents which were composed of ethanol (isopropanol (IPA), dimethyl formamide (DMF)) and

water with different volume ratios. After that, the suspension was sonicated for 10 h. The resultant suspension was centrifuged at 3000 rpm for 10 min to remove the residual layered g-C₃N₄ nanoparticles. Finally, the as-prepared C₃N₄ 2D nanosheets were collected by centrifuging at 10,000 rpm for 5 min and dried at 60 °C in a vacuum oven.

2.2. Characterizations

The as-prepared samples were characterized by powder X-ray diffraction (XRD) on a Bruker D8 Advance X-ray diffractometer operated at 40 kV and 40 mA with Ni-filtered Cu K_α irradiation ($\lambda = 1.5406 \text{ \AA}$). The Fourier transform infrared (FTIR) spectra of products were obtained on a Nicolet Nexus 670 Fourier transform infrared spectrometer at a resolution of 4 cm⁻¹. A total of 64 scans were performed to obtain each spectrum. UV–vis diffuse reflectance spectra (UV–vis DRS) were obtained by using a UV–vis spectrophotometer (Varian Cary 500) and the data were converted to Kubelka–Munk (KM) functions. Barium sulfate was used as a reference. The photoluminescence (PL) spectra were surveyed by an Edinburgh FL/FS900 spectrophotometer with an excitation wavelength at 400 nm. The time-resolved fluorescence decay spectra were surveyed by an Edinburgh FLS980 spectrophotometer with an excitation wavelength at 377 nm and an emission wavelength at 460 nm. The Brunauer–Emmett–Teller (BET) surface area was measured with an ASAP2020 M apparatus (Micromeritics Instrument Corp.). The morphologies of the products were examined by scanning electron microscopy (SEM, FEI Nova NANO-SEM 230 spectrophotometer). Transmission electron microscopy (TEM) images were recorded using a JEOL model JEM 2010 EX microscope at an accelerating voltage of 200 kV. A tapping-mode atomic force microscopy (AFM, Nanoscope Multimode IIIa, Veeco Instruments) with Si-tip cantilever was used to evaluate the morphology of the obtained nanosheets on the mica substrate.

2.3. Electrochemistry measurement

The working electrode was prepared on fluorine-doped tin oxide (FTO) glass, which was cleaned by sonication in chloroform, acetone and ethanol for 30 min. The glass was then rinsed with pure water (18 M Ω cm) and dried in air. The FTO slide was dip coated with 10 μ L of slurry, which was obtained from mixture of 5 mg powder and 0.5 mL dimethylformamide under sonication for 2 h, to get thin film of the samples coated on the FTO slide. After air drying naturally, a copper wire was connected to the side part of the FTO glass using a conductive tape. The uncoated parts of the electrode were isolated with an epoxy resin, and the exposed area of the electrode was 0.25 cm². The electrochemical measurements were performed in a conventional three electrode cell, using a Pt plate and a saturated Ag/AgCl electrode as counter electrode and reference electrode, respectively. The working electrodes were immersed in a 0.2 M Na₂SO₄ aqueous solution without any additive for 30 s before measurement. The photocurrent measurements were conducted with a CHI650E electrochemical workstation (Chenhua

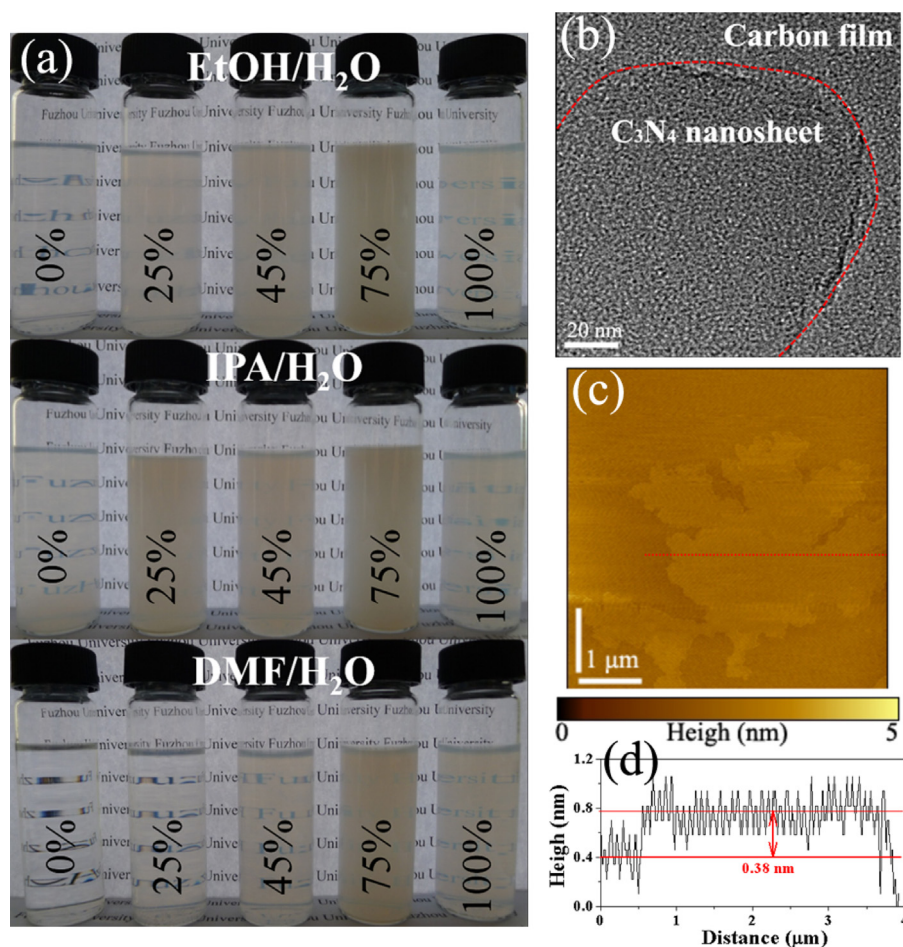


Fig. 2. Photographs of the dispersions of C_3N_4 nanosheets in mixed solvents with different volume ratios of water (a), TEM image (b), AFM image (c) and corresponding cross-sectional profile (d) of typical C_3N_4 nanosheet.

Instruments, Shanghai, China). A 300 W Xe lamp (Beijing Trustech, PLS-SXE300c) with a 420 nm cut-off filter was used as a light source.

2.4. Evaluation of photocatalytic activity

The photocatalytic selective oxidation of benzyl alcohol was performed as follow. A mixture of alcohol (0.1 mmol) and 8 mg of catalyst was dissolved in the solvent of benzotrifluoride (BTF) (1.5 mL), which was saturated with pure molecular oxygen. The choice of solvent BTF is because of its inertness to oxidation and high solubility for molecular oxygen. Then the mixture was transferred into a 10 mL Pyrex glass bottle filled with molecular oxygen at a pressure of 1 bar and stirred to make the catalyst blend evenly in the solution. The suspensions were irradiated by a 300 W Xe lamp (PLS-SXE 300, Beijing Perfectlight Co. Ltd.) with a 420 nm-CUT filter to cut off UV light. After the reaction, the mixture was centrifuged to completely remove the catalyst. The resulting clear liquor was analyzed with an Agilent Gas Chromatograph (GC-6890N). Conversion of alcohol and selectivity for aldehyde were defined as follows:

$$\text{Conversion (\%)} = [(C_0 - C_{\text{alcohol}}) / C_0] * 100$$

$$\text{Selectivity (\%)} = [C_{\text{aldehyde}} / (C_0 - C_{\text{alcohol}})] * 100$$

Where C_0 is the initial concentration of alcohol, and C_{alcohol} and C_{aldehyde} are the concentrations of the residual alcohol and the generated aldehyde, respectively.

For the decomposition of rhodamine B (RhB) in an aqueous solution, the catalyst (40 mg) was suspended in a 100 mL Pyrex glass vessel which contained 80 mL RhB solution (10 ppm). The light source was a 300 W Xe lamp (Beijing Trustech, PLS-SXE300) and a cut-off filter was used to occlude light below 420 nm to ensure the photoreaction proceeded under visible-light irradiation. The suspensions were stirred in the dark for 120 min to ensure adsorption-desorption equilibrium prior to irradiation. During irradiation, 2 mL of the suspension was removed at given time intervals for subsequent RhB concentration analysis following centrifugation. The RhB concentration was analyzed by an UV-vis spectrophotometer (Varian Cary 50).

3. Results and discussion

3.1. Morphology

Fig. 2a showed the photographs of C_3N_4 nanosheet suspensions in different mixed solvents such as ethanol/ H_2O , IPA/ H_2O , and DMF/ H_2O . C_3N_4 nanosheets exhibited significantly different dispersion properties in mixed solvent with different compositions. Taking the ethanol/ H_2O system as a typical example, the concentration of the suspension gradually increased with decreasing the amount of organic solvent, and thereafter, with further increase in the water content, gradual decrease in the concentration was observed. When the volume ratio of water reached 75%, the dispersion of C_3N_4 nanosheet reached its maximum concentration and a “milky” dispersion were obtained. The experimental concentration

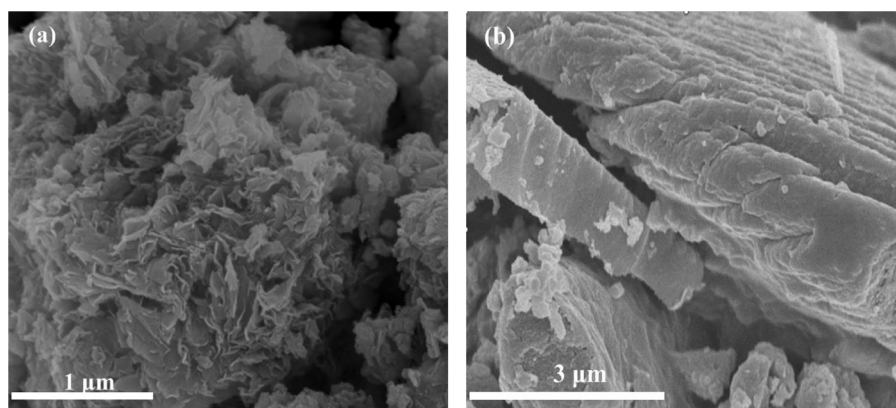


Fig. 3. SEM images of C₃N₄ nanosheet (a) and layered C₃N₄ (b).

was estimated to be 3 mg mL⁻¹. In contrast, the pure organic solvent (~0.2 mg mL⁻¹) and pure water (~0.5 mg mL⁻¹) showed a relatively low concentration. This is a manifestation of the fact that the dispersed concentration is maximised when the energy of exfoliation is minimised. The energy of exfoliation could be represented by the enthalpy of mixing (ΔH_{mix} , per unit volume), which is estimated by a experience equation as follows (Eq. (1)) [35,36]:

$$\frac{\Delta H_{\text{mix}}}{V_{\text{mix}}} \approx \frac{2}{T_{\text{nanosheet}}} (\delta_{\text{nanosheet}} - \delta_{\text{solvent}})^2 \varphi \quad (1)$$

where V is the volume of the suspension, δ is the square root of the component surface energy, T is the average thickness of nanosheet, φ is the nanosheet volume fraction. For the mixed solvents, the surface energy can be tuned by simply changing their compositions. That is, C₃N₄ nanosheets are successfully dispersed in the mixtures of two relatively poor solvents and the concentrations of C₃N₄ nanosheets could be tuned as required. Importantly, the as-prepared suspensions were highly stable, and showed no precipitation after being stored for half a year under ambient conditions. It is worth noting that the C₃N₄ nanosheet powder obtained by a filtered process could be evenly re-dispersed to form a single and stable suspension in aqueous solution, while the bulk g-C₃N₄ powder only produced apparent stratification, as shown in Fig. 1 insert.

TEM image showed that the as-prepared C₃N₄ with laminar morphology exhibited nearly transparent feature, indicating its ultrathin thickness (Fig. 2b). Its lateral scale ranges from sub-micrometer to several micrometers. A Tyndall effect in the suspension (Fig. 1 insert) reveals the presence of highly monodispersed ultrathin C₃N₄ nanosheets in the mixed solvent [3]. The ultrathin thickness was further verified by AFM image, as shown in Fig. 2c. The cross-sectional AFM image shows the uniform thickness of about 0.38 nm. This thickness is well matched with the theoretical value of monolayer C₃N₄ (0.33 nm) [15,17]. This could serve as a strong evidence for the existence of C₃N₄ nanosheet with single atomic layer in the mixed solvents.

The morphology of dried monolayer C₃N₄ nanosheets and layered C₃N₄ were also investigated via SEM. As shown in Fig. 3a, the dried C₃N₄ nanosheet sample still maintained loose and irregular tissue-like 2D nanosheet morphology, although a small portion of C₃N₄ nanosheets was stacked. Its morphology was quite different from that of the parent g-C₃N₄ with a typical layer structure stacked layer by layer (Fig. 3b).

3.2. Structural features

As shown in Fig. 4, for the bulk sample, two characteristic peaks of g-C₃N₄ located at 13.6° for (1 0 0) reflection and 27.4° for (0 0 2)

reflection could be observed [19]. These peaks corresponding to 0.681 and 0.326 nm interlayer spacing are derived from the in-plane repeated units and the stacking of the conjugated aromatic systems in layered structure, respectively [37]. Remarkably, the intensities of these two peaks are significantly decreases after liquid exfoliation. It further verified that the layered g-C₃N₄ has been successfully exfoliated into 2D nanosheet as we expected.

The chemical structure of the C₃N₄ nanosheets was confirmed by the FTIR spectra as shown in Fig. 5A. For the C₃N₄ nanosheets, the sharp peak at 807 cm⁻¹ caused by the breathing vibration of s-triazine ring system was observed [38]. The broad peaks between 3500 and 3000 cm⁻¹ were originated from the N–H and O–H stretches [39], suggesting the free amino groups and adsorbed hydroxyl species on the surface of the nanosheets [34,39]. Characteristic stretching vibration signals of the tri-s-triazine heterocyclic rings were presented in the range of 900–1700 cm⁻¹ [40,41]. The bands observed at 1317 and 1610 cm⁻¹ were related to the C(sp²)–N and C(sp²)=N stretching vibration, respectively [42,43]. It can be seen that the FTIR spectrum of C₃N₄ nanosheets is similar to that of bulk g-C₃N₄, indicating that the C₃N₄ nanosheets still keep the same chemical structure as their parent layered g-C₃N₄.

The resulting samples were further characterized by XPS to reveal their chemical composition and oxidation state, as shown in Fig. 5B–D. There are only three elements (C, N, O) detected in the XPS survey spectra of the samples (Fig. 5B). The O1s peak may be due to the surface absorbed oxygen species, as confirmed by the above FTIR analysis (Fig. 5A). The C₃N₄ nanosheet sample exhibited C1s and N1s signals with a C/N molar ratio of 0.80, close to the ideal C₃N₄ layer composition (C/N=0.75). That is, the chemical composition and the coordination of carbon and nitrogen in C₃N₄ nanosheet are retained during the liquid exfoliation

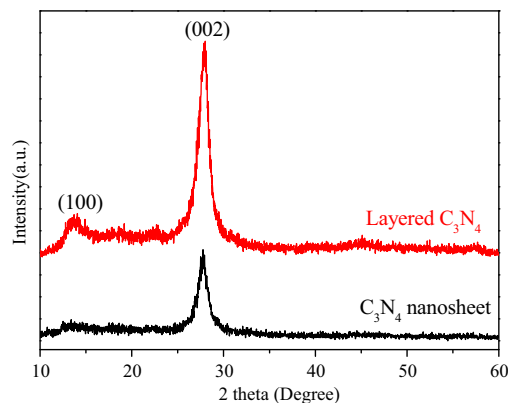


Fig. 4. XRD patterns of layered g-C₃N₄ and C₃N₄ nanosheet.

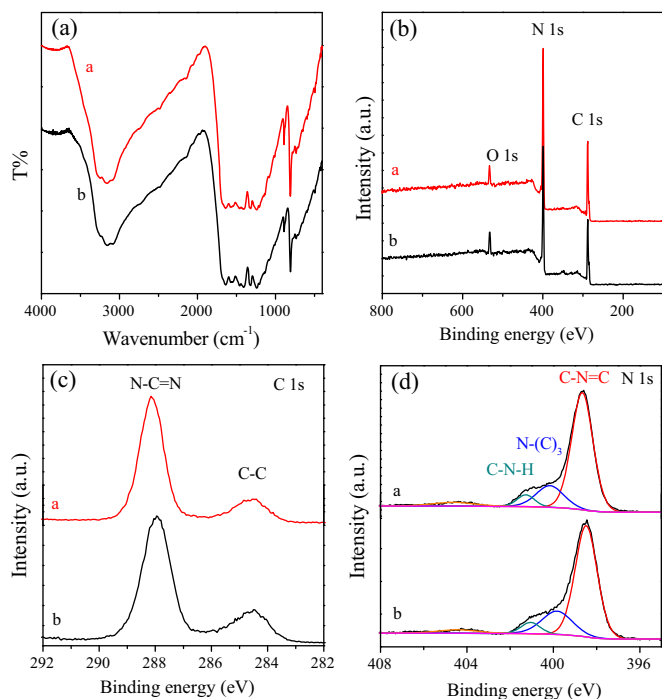


Fig. 5. FTIR (A) and XPS spectra (B–D) of layered C₃N₄ (a) and C₃N₄ nanosheet (b).

process. Furthermore, it also indicated that the organic solvent species adsorbed on the nanosheet's surface could be thoroughly removed during the post-treatment process. The backbone C and N elements in the nanosheet were further investigated by the high resolution spectra. For C 1s spectra (Fig. 5C), there are mainly two carbon species presented in the samples: one (284.6 eV) is sp² C–C bonds, and the other one (288.0 eV) is sp²-hybridized carbon in N-containing aromatic ring (N–C=N) [44]. The latter is considered as the major carbon species in C₃N₄ layer. The high resolution N 1s spectra can be also deconvoluted into four different peaks at binding energies of 398.7, 400.2, 401.3, 404.2 eV, respectively (Fig. 5D). These peaks can be ascribed to the sp²-hybridized nitrogen involved in triazine rings (C–N=C), the tertiary nitrogen N–(C)₃ groups, the free amino groups (C–N–H), and π-excitations, respectively [45].

3.3. Photoabsorption ability

Fig. 6 showed the photoabsorption abilities of the bulk g-C₃N₄ and C₃N₄ nanosheets photocatalysts. Obviously, the samples have a strong absorption in the visible light region. It is worth noting that

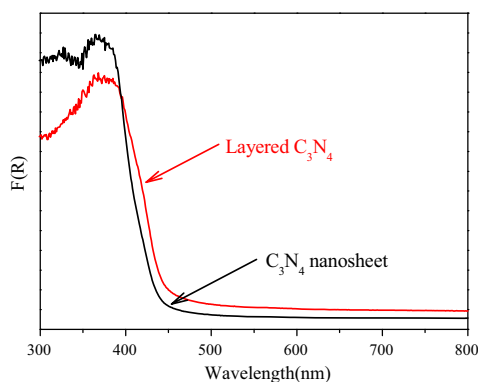


Fig. 6. UV-vis DRS of layered g-C₃N₄ and C₃N₄ nanosheet.

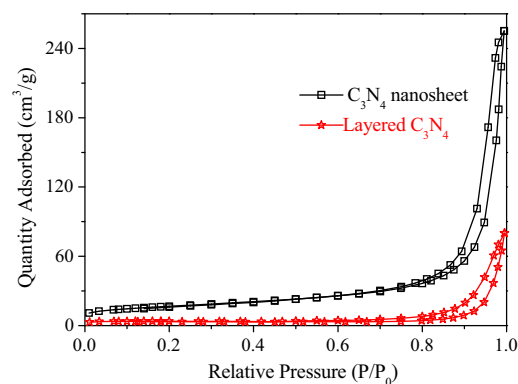


Fig. 7. N₂ adsorption-desorption isotherms of layered g-C₃N₄ and C₃N₄ nanosheet.

C₃N₄ nanosheet showed a lower density of the surface defect sites demonstrated by a less pronounced background level at the same position compared with bulk g-C₃N₄ [46]. The absorption edge of monolayer C₃N₄ nanosheet exhibited a slight blue shift in comparison with the bulk g-C₃N₄. The band gaps of monolayer C₃N₄ nanosheet and bulk g-C₃N₄ were estimated by 2.79 and 2.70 eV, respectively. This may be ascribed to the quantum size effect. The increase in the bandgap by 0.09 eV increased the redox ability of charge carriers generated in the nanosheets.

3.4. BET surface area and porosity

The nitrogen adsorption-desorption isotherms of C₃N₄ nanosheet and bulk g-C₃N₄ revealed that all of the samples exhibited a Type IV adsorption-desorption isotherms with H₃ hysteresis loop in the relative pressure range of 0.6–1.0 (Fig. 7), which were mainly arisen from the mesopores. These mesopores may originate from the stacking of nanosheet. The abrupt closure at a relative pressure of ca. 0.8 suggested the presence of slit-shaped pores, in accordance with the sheet-like shape of the nanostructures. The BET surface area of the C₃N₄ nanosheet is estimated about 59.4 m² g⁻¹, which is about 5 times larger than that of bulk g-C₃N₄ (12.5 m² g⁻¹). The large surface area could provide more reactive sites and adsorb more reactants.

3.5. Photoluminescence

The charge-carriers separation/recombination was monitored by photoluminescence (PL) spectra. As shown in Fig. 8, all of the samples exhibited the obvious PL spectra and the main PL emission peaks appeared at 460 nm, indicating that the π-conjugated system of C₃N₄ nanosheet was not vary after an exfoliation process

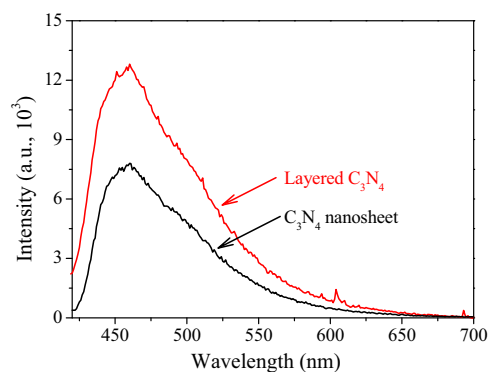


Fig. 8. Photoluminescence spectra under 400 nm excitation at 298 K for layered g-C₃N₄ and C₃N₄ nanosheet.

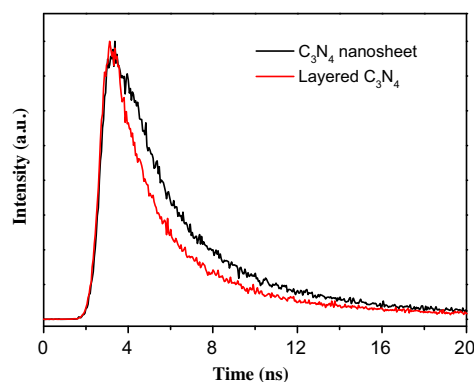


Fig. 9. Time-resolved fluorescence decay spectra of the C_3N_4 nanosheet and layered C_3N_4 .

[17]. Besides, a drastic quenching of the PL intensity over C_3N_4 nanosheet was observed. Because the nanosheet and bulk $g-C_3N_4$ have the same optical absorption performance at 400 nm, we could infer that the recombination of the photogenerated electrons and holes are greatly suppressed in the C_3N_4 nanosheet. It is believed that the increased lifetimes of charge carriers are associated with the improved electron transport and/or electronic band structure changes in the nanosheet.

In order to further understand the photophysical behaviors of photoexcited charge carriers, the time-resolved fluorescence decay spectra of the C_3N_4 nanosheet and layered C_3N_4 were recorded (Fig. 9). The fluorescent intensities of both samples decay exponentially. Clearly, in contrast to the layered C_3N_4 , the C_3N_4 nanosheet showed slower decay kinetics. In other word, the life time of the charge carriers over C_3N_4 nanosheet was longer than that of the layered C_3N_4 . In addition, according to the fitting calculation of the decay spectrum, we got the average charge carriers of the C_3N_4 nanosheet and the layered C_3N_4 were 7.3 ns and 6.4 ns, respectively. It clearly confirmed the recombination of the photo-generated electron and hole is well suppressed in the C_3N_4 nanosheets.

3.6. Photoelectric response

Electrochemical measurements were performed for C_3N_4 nanosheet and the bulk counterpart to further investigate the charge transfer performance. The transient photocurrent responses of the bulk $g-C_3N_4$ and C_3N_4 nanosheet electrodes were recorded for several on-off cycles of intermittent irradiation, as shown in Fig. 10. It could be found that the photocurrent value rapidly

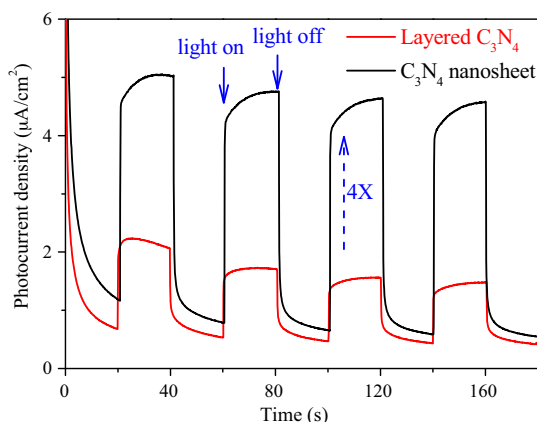


Fig. 10. The periodic on/off photocurrent response of layered $g-C_3N_4$ and C_3N_4 nanosheet electrodes in 0.2 M Na_2SO_4 electrolyte with zero bias versus Ag/AgCl.

Table 1

Photocatalytic activities for selective oxidation of benzyl alcohol over the as-prepared samples with (+)/without (–) visible light irradiation

Entry	Cat.	$h\nu$	Temp./K	Conv./%	Sel./%
1	N-CN ^b	+	298	8.9	>99
2	N-CN	+	313	12.0	>99
3	N-CN	+	333	13.8	>99
4	N-CN	+	353	19.4	>99
5	–	+	298	–	–
6	–	+	353	–	–
7	N-CN	–	298	–	–
8	N-CN	–	353	–	–
9	L-CN ^c	+	298	3.4	>99

^a Reaction conditions: 8 mg cat., 0.1 mmol benzyl alcohol, 1.5 ml benzotrifluoride, O_2 1 bar, 4 h, $\lambda > 420$ nm.

^b C_3N_4 nanosheet.

^c Layered C_3N_4 .

decreased to the initial value as soon as the irradiation of light was off, and the photocurrent came back to a constant value when the light was on again, which was reproducible. That is, the C_3N_4 nanosheet electrodes had steady photoelectrochemical performance under visible light irradiation. It is worth noting that the photocurrent value of $g-C_3N_4$ nanosheets electrode was about 4 times higher than that of the bulk $g-C_3N_4$ electrode. The higher photocurrent value over the C_3N_4 nanosheet electrode resulted from a better electron transfer rate.

3.7. Photocatalytic activities

The photocatalytic activities of the samples were first evaluated by the aerobic oxidations of benzyl alcohol (BA), a well documented model substrate, and conducted under mild temperature and ambient pressure (Table 1). Under visible light irradiation and controlled

temperature at 298 K, C_3N_4 nanosheet showed much higher activity for the aerobic oxidation of BA compared with the bulk counterpart (Table 1, Entries 1 and 9). There was no obvious loss in terms of the photocatalytic activity during five consecutive runs. After the reaction, C_3N_4 nanosheet could be easily separated and reused. Interestingly, when the reaction temperature was increased, the photocatalytic activity of C_3N_4 nanosheet could also be improved obviously (Table 1, Entries 1–4). At 353 K, the conversion of BA reached 19.4% with an extremely high selectivity (>99%). This may be due to the fact that the BA molecules could get over the energy barrier more easily at higher temperature. To confirm the photocatalytic process, we also carried out a set of control experiments. As shown in Table 1, Entries 5 and 6, the self-transformation of BA can be negligible in absence of catalysts under visible light irradiation at 298 and 353 K. Additionally, the thermocatalysis of the nanosheet toward selective oxidation of BA can also be negligible under 298–353 K (Entries 7 and 8).

The as-prepared samples were also used to degrade RhB in aqueous solution under visible light irradiation. Fig. 11a showed that the photolysis of RhB can be negligible. The concentration of RhB did not change in the presence of the catalysts under dark conditions. Therefore, the presence of both visible light and photocatalyst were necessary for the photocatalytic reaction to proceed. Under visible light irradiation, all the catalysts show the obvious photocatalytic activities for discoloration of RhB. Compared with bulk $g-C_3N_4$, the C_3N_4 nanosheet sample prepared by the mixed solvents exhibited much higher degradation rate of RhB. Within 70 min of light irradiation, RhB is degraded almost completely. Moreover, the temporal absorption spectra changes of RhB taken place in

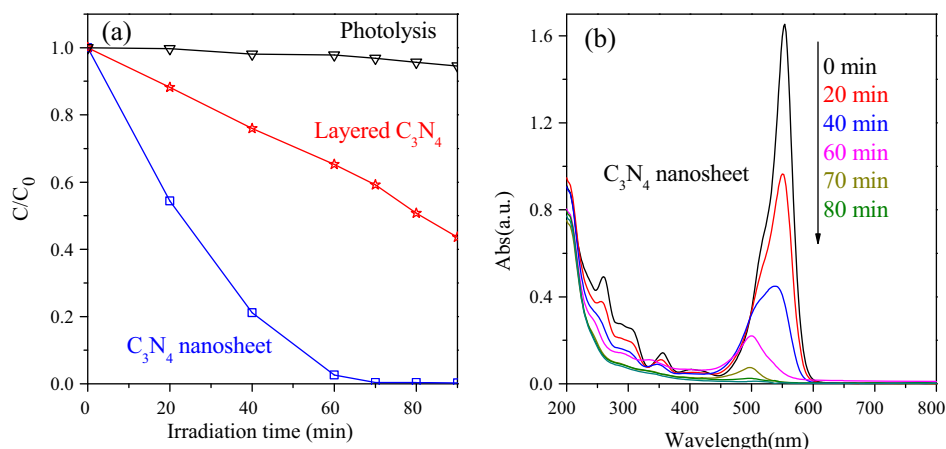


Fig. 11. Photocatalytic activities of layered $\text{g-C}_3\text{N}_4$ and C_3N_4 nanosheet for the degradation of RhB under visible light irradiation.

the presence of C_3N_4 nanosheet were shown in Fig. 11b. Since no new peak appeared, the loss of absorbance could be mainly attributed to the degradation reaction [47]. These observations indicated that the whole conjugated chromophore structure of RhB underwent a facile cleavage. Notably, under visible light irradiation, the absorption maximum of the solution decreased rapidly with a concomitant slight hypsochromic shifts, indicating that a de-ethylation process occurred simultaneously [2,47].

The effect of incident light wavelength on the photocatalytic activity was also investigated, as shown in Fig. 12. The degradation rate of RhB was normalized with the intensity of incident light to exclude the effect of light intensity on the photocatalytic activity. Obviously, we can observe clearly that the degradation rate matched well with the UV-vis DRS of C_3N_4 nanosheet. This is a strong indication that the reaction proceeds catalytically. Moreover, when the incident light wavelengths exceeded 450 nm, C_3N_4 nanosheet still exhibited the photocatalytic activity for the degradation of RhB, although the photoabsorption edge of C_3N_4 nanosheet located at 450 nm. This may be caused by the photosensitization effect of RhB. Therefore, the degradation of RhB over C_3N_4 nanosheet mainly proceeded by the photocatalytic and photosensitized degradation processes.

On the basis of the results of the aforementioned experiments, the improved photocatalytic activities of C_3N_4 nanosheet may be attributed to the synergistic effects of the unique structure characteristics of 2D nanosheet and the photophysical behavior of charge carriers. When the layered $\text{g-C}_3\text{N}_4$ was exfoliated into C_3N_4 nanosheet, the surface area of the sample was greatly enhanced. The large surface area can increase the number of reactive sites for adsorbing abundant reactant molecules. The ultrathin 2D feature of exfoliated nanosheet also made it favorable for reactant

molecules to associate with the monolayer sheets and thus promote interfacial photocatalytic redox reactions with substrates [3]. Furthermore, the atomic thickness could significantly shorten the perpendicular migration distance of the charge carriers from the bulk to the surface [13], as shown in Fig. 13b. Considering the high in-plane conductivity and low surface defects of C_3N_4 nanosheet, once charge carriers were excited, the atomic structure sensitively affected the carrier transfer process in the 2D system, resulting in the consequent reduction of the recombination probability and

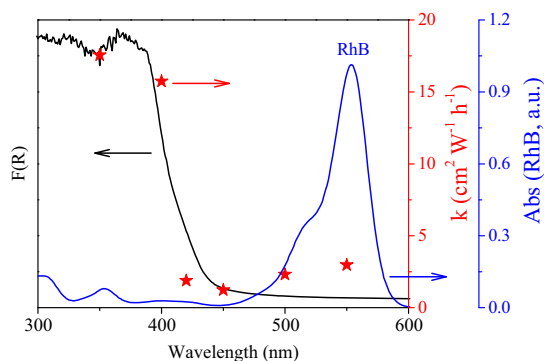


Fig. 12. Wavelength-dependent the degradation of RhB by $\text{g-C}_3\text{N}_4$ nanosheet.

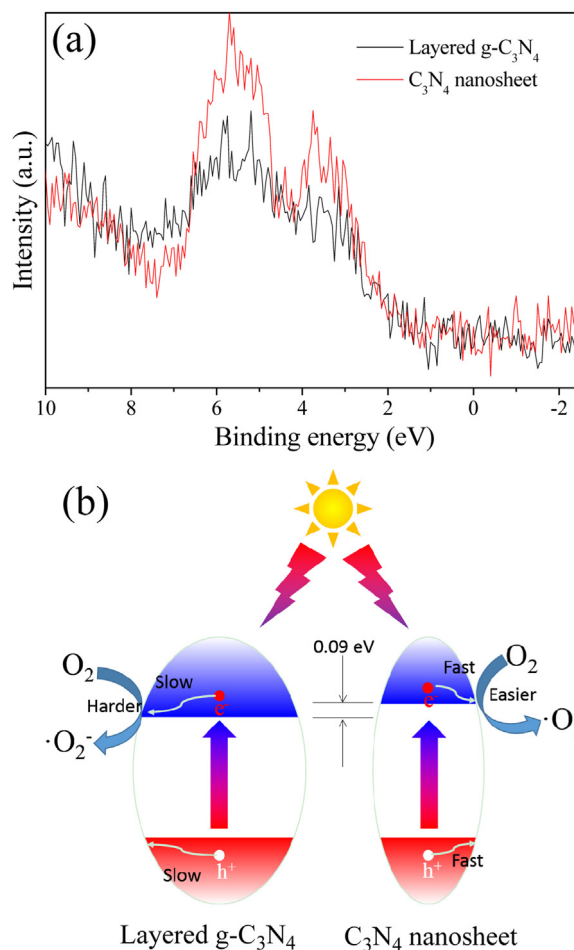


Fig. 13. VB XPS spectra (a) and schematic illustration of electron-hole separation and transport (b) of layered $\text{g-C}_3\text{N}_4$ and C_3N_4 nanosheet.

prolongation of the lifetime of photogenerated electron-hole pairs. Finally but importantly, the monolayer nanosheet with strong quantum size effect induced an increase of the surface disorder. That is, the electronic properties of the nanosheets would be inevitably influenced. Fig. 13a showed that the VB maxima of layered g-C₃N₄ and C₃N₄ nanosheet at the same level were estimated to be 1.83 eV. Combining with DRS results, the conduction band (CB) potential of C₃N₄ nanosheet was shifted by 0.09 eV toward more negative. For C₃N₄ nanosheet, the photogenerated electron with higher reduction ability could facilitate the generation of $\cdot\text{O}_2^-$ radicals (Fig. 13b). It is well documented that $\cdot\text{O}_2^-$ and photogenerated hole as the primary active species in the photocatalytic reactions over g-C₃N₄ photocatalyst [48–50]. Due to the functionalities of C₃N₄ nanosheet inherited from the parent g-C₃N₄, the higher concentration of $\cdot\text{O}_2^-$ would lead to the higher photocatalytic performances of C₃N₄ nanosheet toward the oxidation of alcohols and RhB.

4. Conclusions

In conclusion, monolayer C₃N₄ nanosheets have been successfully prepared by a versatile and scalable mixed solvent strategy for the first time. Two poor solvents can be combined into good solvents for efficiently exfoliating bulk g-C₃N₄ into C₃N₄ nanosheets. Importantly, the concentration of C₃N₄ nanosheets could be tunable by simply adjusting the volume ratio of solvents. The as-prepared C₃N₄ nanosheet sample was free-standing and still retained the structural features of g-C₃N₄ layer. Furthermore, the C₃N₄ nanosheet with the exceptionally high 2D anisotropy would be also endowed novel electronic structures and distinctive physicochemical properties, such as favorable band structure, high electron mobility, prolonged photogenerated charge lifetime, atomic thickness, extremely high percentage of exposed active sites, high specific surface area, and low surface defects. All these favorable factors facilitate the photocatalytic reactions over C₃N₄ nanosheets. Thus, the as-prepared C₃N₄ nanosheets showed superior photocatalytic activities for both selective oxidation of benzyl alcohol and degradation of RhB under visible light irradiation compared with its bulk counterpart. We anticipate that the mixed-solvent method could also be used to exfoliate other layered materials to produce 2D nanosheets. And thus, it may provide new opportunities for enlarging the family of photocatalysts.

Acknowledgements

The work was supported by the National Natural Science Foundation of China (21303019, 21177024 and 21273036), the National Science Foundation of Fujian Province (2014J05016) and the Research Foundation for Middle-age and Young Teachers of Fujian Province (JA13055). We also thank Prof. Quanming Wang from Xiamen University for the time-resolved fluorescence decay spectra measurements.

References

- [1] M. Chhowalla, H.S. Shin, G. Eda, L.-J. Li, K.P. Loh, H. Zhang, *Nat. Chem.* 5 (2013) 263–275.
- [2] S. Liang, R. Liang, L. Wen, R. Yuan, L. Wu, X. Fu, *Appl. Catal. B* 125 (2012) 103–110.
- [3] S. Liang, L. Wen, S. Lin, J. Bi, P. Feng, X. Fu, L. Wu, *Angew. Chem. Int. Ed.* 53 (2014) 2951–2955.
- [4] M. Osada, T. Sasaki, *J. Mater. Chem.* 19 (2009) 2503–2511.
- [5] M. Osada, T. Sasaki, *Adv. Mater.* 24 (2012) 210–228.
- [6] Q.H. Wang, K. Kalantar-Zadeh, A. Kis, J.N. Coleman, M.S. Strano, *Nat. Nanotechnol.* 7 (2012) 699–712.
- [7] H. Li, J. Wu, Z. Yin, H. Zhang, *Accounts. Chem. Res.* 47 (2014) 1067–1075.
- [8] X. Peng, L. Peng, C. Wu, Y. Xie, *Chem. Soc. Rev.* 43 (2014) 3303–3323.
- [9] Y. Sun, S. Gao, Y. Xie, *Chem. Soc. Rev.* 43 (2014) 530–546.
- [10] R. Ma, T. Sasaki, *Adv. Mater.* 22 (2010) 5082–5104.
- [11] S.Z. Butler, S.M. Hollen, L. Cao, Y. Cui, J.A. Gupta, H.R. Gutiérrez, T.F. Heinz, S.S. Hong, J. Huang, A.F. Ismach, E. Johnston-Halperin, M. Kuno, V.V. Plashnitsa, R.D. Robinson, R.S. Ruoff, S. Salahuddin, J. Shan, L. Shi, M.G. Spencer, M. Terrones, W. Windl, J.E. Goldberg, *ACS Nano* 7 (2013) 2898–2926.
- [12] K.J. Koski, Y. Cui, *ACS Nano* 7 (2013) 3739–3743.
- [13] R. Mas-Balleste, C. Gomez-Navarro, J. Gomez-Herrero, F. Zamora, *Nanoscale* 3 (2011) 20–30.
- [14] G. Pacchioni, *Chem.–Eur. J.* 18 (2012) 10144–10158.
- [15] D.S. Su, J. Zhang, B. Frank, A. Thomas, X. Wang, J. Paraknowitsch, R. Schlögl, *ChemSusChem* 3 (2010) 169–180.
- [16] X. Wang, S. Blechert, M. Antonietti, *ACS Catal.* 2 (2012) 1596–1606.
- [17] Y. Wang, X. Wang, M. Antonietti, *Angew. Chem. Int. Ed.* 51 (2012) 68–89.
- [18] A. Thomas, A. Fischer, F. Goettmann, M. Antonietti, J.-O. Müller, R. Schlögl, J.M. Carlsson, *J. Mater. Chem.* 18 (2008) 4893–4908.
- [19] X. Wang, K. Maeda, A. Thomas, K. Takanebe, G. Xin, J.M. Carlsson, K. Domen, M. Antonietti, *Nat. Mater.* 8 (2009) 76–80.
- [20] X. Wang, K. Maeda, X. Chen, K. Takanebe, K. Domen, Y. Hou, X. Fu, M. Antonietti, *J. Am. Chem. Soc.* 131 (2009) 1680–1681.
- [21] G. Liu, P. Niu, C. Sun, S.C. Smith, Z. Chen, G.Q. Lu, H.-M. Cheng, *J. Am. Chem. Soc.* 132 (2010) 11642–11648.
- [22] Y. Wang, J. Zhang, X. Wang, M. Antonietti, H. Li, *Angew. Chem. Int. Ed.* 49 (2010) 3356–3359.
- [23] J. Zhang, J. Sun, K. Maeda, K. Domen, P. Liu, M. Antonietti, X. Fu, X. Wang, *Energy Environ. Sci.* 4 (2011) 675–678.
- [24] J. Zhang, G. Zhang, X. Chen, S. Lin, L. Möhlmann, G. Dolega, G. Lipner, M. Antonietti, S. Blechert, X. Wang, *Angew. Chem. Int. Ed.* 51 (2012) 3183–3187.
- [25] Y. Hou, A.B. Laursen, J. Zhang, G. Zhang, Y. Zhu, X. Wang, S. Dahl, I. Chorkendorff, *Angew. Chem. Int. Ed.* 52 (2013) 3621–3625.
- [26] P. Niu, L. Zhang, G. Liu, H.-M. Cheng, *Adv. Funct. Mater.* 22 (2012) 4763–4770.
- [27] X. Zhang, X. Xie, H. Wang, J. Zhang, B. Pan, Y. Xie, *J. Am. Chem. Soc.* 135 (2012) 18–21.
- [28] S. Yang, Y. Gong, J. Zhang, L. Zhan, L. Ma, Z. Fang, R. Vajtai, X. Wang, P.M. Ajayan, *Adv. Mater.* 25 (2013) 2452–2456.
- [29] J. Tian, Q. Liu, C. Ge, Z. Xing, A.M. Asiri, A.O. Al-Youbi, X. Sun, *Nanoscale* 5 (2013) 8921–8924.
- [30] J. Tian, Q. Liu, A.M. Asiri, A.H. Qusti, A.O. Al-Youbi, X. Sun, *Nanoscale* 5 (2013) 11604–11609.
- [31] H. Xu, J. Yan, X. She, L. Xu, J. Xia, Y. Xu, Y. Song, L. Huang, H. Li, *Nanoscale* 6 (2014) 1406–1415.
- [32] H. Zhao, H. Yu, X. Quan, S. Chen, H. Zhao, H. Wang, *RSC Adv.* 4 (2014) 624–628.
- [33] X. She, H. Xu, Y. Xu, J. Yan, J. Xia, L. Xu, Y. Song, Y. Jiang, Q. Zhang, H. Li, *J. Mater. Chem. A* 2 (2014) 2563–2570.
- [34] B.V. Lotsch, M. Döblinger, J. Sehnert, L. Seyfarth, J. Senker, O. Oeckler, W. Schnick, *Chem. Eur. J.* 13 (2007) 4969–4980.
- [35] Y. Hernandez, V. Nicolosi, M. Lotya, F.M. Blighe, Z. Sun, S. De, I.T. McGovern, B. Holland, M. Byrne, Y.K. Gun'ko, J.J. Boland, P. Niraj, G. Duesberg, S. Krishnamurthy, R. Goodhue, J. Hutchison, V. Scardaci, A.C. Ferrari, J.N. Coleman, *Nat. Nanotechnol.* 3 (2008) 563–568.
- [36] J.N. Coleman, M. Lotya, A. O'Neill, S.D. Bergin, P.J. King, U. Khan, K. Young, A. Gaucher, S. De, R.J. Smith, I.V. Shvets, S.K. Arora, G. Stanton, H.-Y. Kim, K. Lee, G.T. Kim, G.S. Duesberg, T. Hallam, J.J. Boland, J.J. Wang, J.F. Donegan, J.C. Grunlan, G. Moriarty, A. Shmeliov, R.J. Nicholls, J.M. Perkins, E.M. Grieveson, K. Theuwissen, D.W. McComb, P.D. Nellist, V. Nicolosi, *Science* 331 (2011) 568–571.
- [37] X. Zhang, X. Chen, A. Thomas, X. Fu, M. Antonietti, *Adv. Mater.* 21 (2009) 1609–1612.
- [38] Q. Xiang, J. Yu, M. Jaroniec, *J. Phys. Chem. C* 115 (2011) 7355–7363.
- [39] Y. Li, J. Zhang, Q. Wang, Y. Jin, D. Huang, Q. Cui, G. Zou, *J. Phys. Chem. B* 114 (2010) 9429–9434.
- [40] V.N. Khabashesku, J.L. Zimmerman, J.L. Margrave, *Chem. Mater.* 12 (2000) 3264–3270.
- [41] G. Zhang, J. Zhang, M. Zhang, X. Wang, *J. Mater. Chem.* 22 (2012) 8083–8091.
- [42] K. Schwinghammer, B. Tuffy, M.B. Mesch, E. Wirnhier, C. Martineau, F. Taulelle, W. Schnick, J. Senker, B.V. Lotsch, *Angew. Chem. Int. Ed.* 52 (2013) 2435–2439.
- [43] K. Schwinghammer, M.B. Mesch, V. Duppel, C. Ziegler, J. Senker, B.V. Lotsch, *J. Am. Chem. Soc.* 136 (2014) 1730–1733.
- [44] J. Zhang, M. Zhang, G. Zhang, X. Wang, *ACS Catal.* 2 (2012) 940–948.
- [45] B. Long, J. Lin, X. Wang, *J. Mater. Chem. A* 2 (2014) 2942–2951.
- [46] Y. Chen, S. Liang, L. Wen, W. Wu, R. Yuan, X. Wang, L. Wu, *Phys. Chem. Chem. Phys.* 15 (2013) 12742–12747.
- [47] S. Liang, S. Zhu, Y. Chen, W. Wu, X. Wang, L. Wu, *J. Mater. Chem.* 22 (2012) 2670–2678.
- [48] S.C. Yan, Z.S. Li, Z.G. Zou, *Langmuir* 26 (2010) 3894–3901.
- [49] Y. Cui, Z. Ding, X. Fu, X. Wang, *Angew. Chem. Int. Ed.* 51 (2012) 11814–11818.
- [50] X. Bai, R. Zong, C. Li, D. Liu, Y. Liu, Y. Zhu, *Appl. Catal. B* 147 (2014) 82–91.